J. Plasma Phys. (2026), *vol*. 92, E114 © The Author(s), 2026. Published by Cambridge University Press. This is an Open Access article, distributed under the terms of the Creative Commons Attribution licence (https://creativecommons.org/licenses/by/4.0/), which permits unrestricted re-use, distribution and reproduction, provided the original article is properly cited. doi:10.1017/S002237782610213X

Convective parametric instabilities in inhomogeneous plasmas: revisit using exact WKB approach

Taotao Zhou[1,2], Nong Xiang[1], Chunyun Gan[1], Tianyang Xia[1] and Zhiyong Qiu[1]

[1]Institute of Plasma Physics, Hefei Institutes of Physical Science, Chinese Academy of Sciences, Hefei 230031, PR China

[2]University of Science and Technology of China, Hefei 230026, PR China

Corresponding author: Zhiyong Qiu, zqiu@ipp.ac.cn

(Received 4 April 2026 UTC; revision received 15 June 2026 UTC; accepted 7 July 2026 UTC)

We revisit parametric instability (PI) in inhomogeneous plasma using the exact Wentzel–Kramers–Brillouin (WKB) method applied to the coupled daughter-wave equations. Both resonant and non-resonant regimes, as well as forward and backward scattering, are examined. Compared with the previously adopted conventional WKB approach, the exact WKB approach explicitly incorporates boundary conditions and Stokes jumps, providing a more complete description of mode evolution. Consequently, all four PI regimes exhibit a universal daughter-wave amplification factor $|V_r|/\epsilon$, where V_r corresponds to the real part of the Voros multiplier associated with the turning-point pair and ϵ is the strength of inhomogeneity. The exact WKB method resolves the vanishing-growth prediction for resonant backward scattering PI obtained in the conventional WKB approach, which neglects Stokes jumps. Furthermore, exact WKB analysis shows that the inverse dependence of the amplification factor on inhomogeneity is insensitive to ϵ, provided that the combined wave equation reduces to a Weber-type equation. These results highlight the capability of the exact WKB framework to study PIs beyond the validity conditions of the conventional WKB approach, providing explicit physical insights inaccessible to numerical approaches.

Key words: plasma waves, plasma nonlinear phenomena, fusion plasma

1. Introduction

Parametric instability (PI) is a ubiquitous phenomenon in nonlinear wave systems, arising from the nonlinear interaction among a strong pump wave and two daughter waves (Chen 1984). When the wavenumber and frequency of the three waves satisfy the matching condition, and the pump intensity exceeds a threshold, the pump will transfer energy to the daughter waves, resulting in exponential growth of the daughter waves.

Downloaded from https://www.cambridge.org/core. UNIVERSIDAD AUTONOMA METROPOLITANA, on 19 Nov 2026 at 15:26:59, subject to the Cambridge Core terms of use, available at https://www.cambridge.org/core/terms. https://doi.org/10.1017/S002237782610213X

PI plays an important role in plasma physics and controlled fusion experiments (Liu & Tripathi 1985). In magnetic fusion, for instance, radio-frequency wave injection is widely employed for plasma heating and toroidal current drive (Fisch 1987), typically designed based on the linear and quasi-linear behaviour of waves. However, as the plasma parameters approach fusion reactor level (Qiu *et al.* 2025) and the required wave power injection increases, PI-driven daughter waves are generated, leading to pump energy depletion, and may further trigger undesired phenomena beyond the intended design (Xiang & Cary 2008; Ding *et al.* 2018; Yan *et al.* 2024). Similarly, in inertial confinement fusion, PI in the form of stimulated Raman or Brillouin scattering can reduce laser energy coupling efficiency and compromise compression uniformity, generating backward daughter waves such as plasma waves and producing non-thermal electrons (Hellwarth 1963; Afeyan & Williams 1995).

Models for predicting and controlling PI have been extensively developed over the past decades. They can be classified according to their physical fidelity and treatment of spatial and nonlinear effects. At the simplest level, local growth-rate models based on parametric dispersion relations in homogeneous plasmas (Porkolab 1970; Porkoláb 1972; Liu & Tripathi 1985) provide rapid estimates of instability thresholds (Liu *et al.* 1984) and parameter dependencies (Zhao & Gao 2013; Yang & Gao 2025). Extending this approach, gain-integral (Rosenbluth 1972) and WKB-type (White *et al.* 1974) models allow distinction between convective and absolute instabilities (Picard & Johnston 1983). These models are most widely used because they can incorporate effects such as weak plasma inhomogeneity (Li *et al.* 2024; Chen & Gao 2025), finite pump length (Chen & Berger 1977; Cesario *et al.* 2006) and altered wave trajectories (Huang *et al.* 2026). Beyond these, full-wave simulations based on the governing partial differential equations capture broadband spectra and wave propagation effects, albeit often in reduced dimensionality (Napoli *et al.* 2013; Castaldo & Napoli 2024). Reduced nonlinear models, such as three-wave coupling equations (Kaup, Reiman & Bers 1979; Reiman 1979), provide a more energy-conserving description, capturing both pump depletion and saturation dynamics. At the highest level of fidelity, kinetic simulations with particle-in-cell methods (Bao *et al.* 2016; Zhou *et al.* 2022), self-consistently incorporate wave–particle interactions and nonlinear feedback, albeit at the cost of substantial computational cost. Finally, for incoherent or broadband drivers, statistical models are employed to describe phase randomness and spectral effects (DuBois, Bezzerides & Rose 1992; Ma *et al.* 2021).

Among these models, the WKB approximation (Bahar 1967) is a commonly used analytical tool in reducing PI coupling models. Within this framework, the wave field is represented as a product of a slowly varying amplitude and an exponential of a rapidly varying phase, typically written as $\exp(i\int^x k(x)\mathrm{d}x)/\sqrt{k(x)}$, where $k(x)$ denotes the local wavenumber. However, as an asymptotic approximation, the conventional WKB expansion becomes divergent in regions where its validity condition $|k|^2 \gg \epsilon$ breaks down. Here, ϵ characterises the scale of background inhomogeneity. Furthermore, the conventional WKB framework relies on wavenumbers predicted by the linear wave equations, whereas in wave–wave coupling regions, it cannot capture nonlinear modifications to the wavenumbers (Qiu, Chen & Zonca 2014), leading to a biased understanding of underlying dynamics.

The exact WKB method (Kawai & Takei 2005; Iwaki 2024), originally developed in the mathematical analysis of linear differential equations (Balian, Parisi & Voros 1978; Voros 1983), has undergone substantial development in recent decades in high-energy physics (Sueishi *et al.* 2020, 2021) and quantum mechanics

Downloaded from https://www.cambridge.org/core. UNIVERSIDAD AUTONOMA METROPOLITANA, on 19 Nov 2026 at 15:26:59, subject to the Cambridge Core terms of use, available at https://www.cambridge.org/core/terms. https://doi.org/10.1017/S002237782610213X

(Yan 2022; Ito & Yang 2024; Suzuki, Taniguchi & Iwamura 2024). It provides a systematic framework for overcoming the limitations of conventional WKB. The method was first established for Airy-like equations (Voros 1983; Kawai & Takei 2005), subsequently extended to second-order Schrödinger-type equations with polynomial potentials (Takei 2017; Ito, Mariño & Shu 2019; Nemes 2021) and has recently been generalised to higher-order ordinary differential equations (ODEs) with varying coefficients (Honda, Kawai & Takei 2015; Nemes 2025). By employing the Borel–Padé resummation technique to reconstruct convergent solutions from the formal WKB expansions, the exact WKB method yields globally defined solutions on the complex plane. These solutions asymptotically reduce to the familiar conventional WKB forms away from turning points, while near the turning points, their discontinuous behaviour is governed by the Stokes diagrams and connection formulae. Consequently, exact WKB retains the clear physical interpretation of conventional WKB while achieving quantitative exact solutions, thereby providing a distinctive analytical framework for the study of PIs.

Since its development, exact-WKB analysis has been successfully applied to a wide range of physical problems, in which physically observable quantities can often be understood in terms of exact-WKB structures such as Stokes phenomena, Voros multipliers and connection formulae. For example, in quantum spectral problems involving double-well (Kamata *et al.* 2023) and periodic-well potentials (Dunne & Ünsal 2017; Imaizumi 2020), Voros multipliers are closely related to quantum periods (Codesido & Mariño 2018), Floquet effective Hamiltonian (Fujimori *et al.* 2025) and non-perturbative instanton contributions (Zinn-Justin 1981). In black-hole perturbation theory, reflection and transmission coefficients can be determined through the connection formulae (Konoplya, Zhidenko & Zinhailo 2019; Miyachi *et al.* 2025). In cosmology, particle-pair production from the vacuum can be interpreted as a manifestation of the Stokes phenomenon (Taya *et al.* 2021; Enomoto & Matsuda 2023). In the context of PI considered here, similar physical interpretations emerge. We shall show that the Voros multiplier is directly connected to the exponential amplification factor of daughter waves, while the Stokes phenomena may correspond to the abrupt onset of a daughter wave or quasi-mode. The connection formula is the key in determining daughter-wave amplitudes across different spatial regions.

To facilitate practical applications, we have developed a Mathematica–MATLAB code that combines the symbolic computation capabilities of Mathematica with the data visualisation functionality of MATLAB. As an initial step in code validation, we revisit a prototypical problem: convective PI in inhomogeneous plasmas. This system admits four distinct regimes: resonant forward scattering, resonant backward scattering, non-resonant forward scattering and non-resonant backward scattering. The classification into resonant and non-resonant regimes is determined by the second daughter wave (denoted as 'u'), while the other daughter wave (denoted as '1') is always resonant. Forward (backward) scattering refers to the case where the two daughter waves propagate in the same (opposite) directions. To the best of our knowledge, this work also represents the first application of the exact WKB method to plasma physics.

This problem was previously studied by the authors, who proposed an approach that first combines the two daughter-wave equations into a single ODE and then solves the ODE using the conventional WKB method (Zhou *et al.* 2025). In this work, we revisit this problem using the exact WKB method instead. Mathematically, the resulting ODE is equivalent to a Weber-type equation, a class of problems that

Downloaded from https://www.cambridge.org/core. UNIVERSIDAD AUTONOMA METROPOLITANA, on 19 Nov 2026 at 15:26:59, subject to the Cambridge Core terms of use , available at https://www.cambridge.org/core/terms. https://doi.org/10.1017/S002237782610213X

has already been extensively investigated within the framework of exact WKB analysis (Sueishi *et al.* 2020, 2021; Fujimori *et al.* 2025). Our interest here is therefore not in the mathematical solution itself, but in the physical insights that the exact WKB framework can provide for PI.

We will see that for PI problems, conventional WKB may fail in backward scattering regimes due to its inability to enforce boundary conditions for daughter waves incident from both sides, whereas numerical approaches often obscure the underlying wave structure. Exact WKB overcomes these limitations by providing globally defined eigenmodes that can reduce to a simple WKB-type wave description far from the turning points while retaining full accuracy near them.

The rest of this work is organised as follows. Section 2 provides a concise review of the conventional WKB approach applied to four types of PIs, including the reduction of the two daughter-wave equations into a single ODE. Section 3 presents the exact WKB method as a systematic procedure for solving Schrödinger-like equations. In § 4, we apply the exact WKB method to the four types of convective PIs in inhomogeneous plasmas and compare the results with those obtained from conventional WKB. A unified formula for the PI amplification factor of all four types will be presented. Finally, § 5 summarises the main results and discusses the PI amplification factor in strong inhomogeneity.

2. Brief review of conventional WKB approach

Considering a PI process in which a fixed-amplitude pump wave with frequency and wavenumber (ω_0, k_0) decays into a propagating wave (ω_1, k_1) and another wave (ω_u, k_u) in an inhomogeneous plasma, the simplest first-order form of the governing daughter-wave equations is given by

$$\phi_u' - iK_u\phi_u = \frac{\Gamma}{v_{gu}} e^{iK_0x}\phi_1, \tag{2.1}$$

$$\phi_1' - iK_1\phi_1 = \frac{\Gamma^*}{v_{g1}} e^{-iK_0x}\phi_u. \tag{2.2}$$

Here, Γ is the nonlinear coupling coefficient, v_{g1} and v_{gu} are the group velocities of the daughter waves, $\phi_1(x)$ and $\phi_u(x)$ are wave functions of daughter waves 'u' and '1', respectively, and ϕ' represents spatial differentiation $(\mathrm{d}/\mathrm{d}x)\phi(x)$. The linear wavenumbers of the pump, daughter 'u' and daughter '1' waves are denoted by K_0, K_u, K_1, respectively. Here, we focus on a prototype PI problem (Rosenbluth 1972) that captures the effect of wavenumber mismatch on the PI process, where we take $K_1(x) = \epsilon x$ and assume all other parameters are approximately spatially uniform. In the conventional WKB framework, the inhomogeneity ϵ should be weak by $\epsilon \leqslant \max(|K_j|^2)$, with $j = u, 0, 1$.

Taking a rescaling transformation $x \to x/\epsilon$, (2.1) and (2.2) can be combined into a second-order ODE with respect to ϕ_1 as

$$\epsilon^2\phi_1'' + i(K_0 - K_u - x)\epsilon\phi_1' + \left[(K_0 - K_u)\,x - \frac{|\Gamma|^2}{v_{g1}v_{gu}} - i\epsilon\right]\phi_1 = 0. \tag{2.3}$$

In conventional WKB, this equation can be directly written into a local parametric dispersion relation form by taking $\partial_x \simeq (iK_1 + \gamma_{k1})/\epsilon$, and we obtain

$$\mathrm{Re}(\gamma_{k1}) = -\frac{1}{2}K_{ui} + \mathrm{sgn}(v_{gu}v_{g1})\mathrm{Re}\left[\sqrt{\frac{|\Gamma|^2}{v_{gu}v_{g1}} + i\epsilon - \frac{1}{4}(K_u - K_0 - x)^2}\right], \tag{2.4}$$

Downloaded from https://www.cambridge.org/core. UNIVERSIDAD AUTONOMA METROPOLITANA, on 19 Nov 2026 at 15:26:59, subject to the Cambridge Core terms of use, available at https://www.cambridge.org/core/terms. https://doi.org/10.1017/S002237782610213X

where Re indicates the real part, γ_{k1} denotes the slowly amplitude evolution in x and K_{ui} is the imaginary part of K_u. The amplification factor of wave '1' is defined as the logarithm of the difference in the daughter-wave amplitude between the probe point and the noise-seeding point. The seeding point is generally chosen at the location that yields the maximal amplitude contrast. Here, the maximal magnitude difference is obtained by integrating (2.4) from $-\infty$ to $+\infty$, resulting in

$$A_{\mathrm{inhom}} = \begin{cases} -\left[\dfrac{2|\Gamma|^2}{\epsilon v_{gu} v_{g1}} \operatorname{asin}\left(\dfrac{-K_{ui}}{2\sqrt{-|\Gamma|^2/v_{gu}v_{g1}}}\right) + \dfrac{K_{ui}}{\epsilon}\sqrt{-\dfrac{|\Gamma|^2}{v_{gu}v_{g1}} - \dfrac{K_{ui}^2}{4}}\right] & \text{(nearly) resonant backward scattering,} \\ \dfrac{\pi|\Gamma|^2}{\epsilon v_{gu} v_{g1}} & \text{elsewise.} \end{cases} \tag{2.5}$$

This unified formalism is a more precise version of (48) in our previous work (Zhou *et al.* 2025). For most types of PI, the amplification factor conserves at simple form $(\pi|\Gamma|^2)/(\epsilon v_{gu} v_{g1})$, except for the backward scattering resonant PI and its intermediate state transiting into non-resonant, and this special regime satisfies $K_{ui} \leqslant 0$, $v_{gu} v_{g1} < 0$, and $|K_{ui}| < 2\sqrt{|\Gamma|^2/|v_{gu} v_{g1}|}$.

3. Recipe of exact WKB

As exact WKB provides a clearer wave picture and exact solutions beyond the validity condition of conventional WKB, we use it to study the four types of PI by solving (2.3). Since this is its first application to plasma physics, we present a brief recipe as follows.

Consider a general one-dimensional Schrödinger-type equation

$$\delta^2 \frac{\mathrm{d}^2\phi(x)}{\mathrm{d}x^2} - Q(x)\phi(x) = 0, \tag{3.1}$$

where δ is a small parameter. The WKB solution is in a form $\phi(x) = \exp[\int^x S\,\mathrm{d}x]$, where the Ricatti-WKB coefficient $S \equiv \sum_{n=-1}^{\infty} \delta^n S_n$ can be solved order by order as

$$S_{-1}^{\pm} = \pm\sqrt{Q},\ S_0^{\pm} = -\frac{Q'}{4Q},\ S_1^{\pm} = \pm\frac{4QQ'' - 5Q'^2}{32Q^{5/2}}, \cdots . \tag{3.2}$$

Conventional WKB relies on approximate truncation of the above-mentioned series; the eigenfunctions can be obtained by keeping the first two terms as

$$\phi_{\mathrm{C}}^{\pm} = \frac{\exp(\pm\int^x \delta^{-1}\sqrt{Q}\,\mathrm{d}x)}{Q^{1/4}}. \tag{3.3}$$

When $Q(x) \to 0, \infty$ or when δ becomes large, the WKB approximation breaks down and the expansion becomes divergent.

In exact WKB, this limitation can be overcome by resumming the divergent series into a convergent one, including steps such as Borel resummation $\mathcal{B}$, Padé approximation and inverse-Laplacian transformation $\mathcal{L}^{-1}$. Details of this technique

Downloaded from https://www.cambridge.org/core. UNIVERSIDAD AUTONOMA METROPOLITANA, on 19 Nov 2026 at 15:26:59, subject to the Cambridge Core terms of use, available at https://www.cambridge.org/core/terms. https://doi.org/10.1017/S002237782610213X

can be found from Kawai & Takei (2005, Chapter 1). For any divergent series $S=\sum_{n=0}^{\infty}\delta^n S_n$, we note its well-resumed value as $\mathcal{L}^{-1}\mathcal{B}[S]$.

The convergence of the resummed WKB series enables the construction of exact WKB eigen-solutions that reduce to the conventional WKB approximation in its domain of validity while remaining exact elsewhere. Although these solutions are discontinuous across Stokes lines, the discontinuities obey a simple universal connection formula. In practice, one first constructs the Stokes diagram, then determines the exact WKB solutions in each Stokes sector and fixes their coefficients via boundary or initial conditions. The global solution is obtained by tracking the Stokes transitions along a given path and solving the resulting connection formula.

The detailed procedure takes the following steps.

3.1. *Construction of the Stokes diagram*

Stokes diagram provides a graphical representation illustrating how WKB solutions change dominance across different regions in the complex $\mathbb{C}$ plane and the detailed construction includes the following. (i) Determining the turning points x_t by solving $Q(x_t)=0$. (ii) Plotting the Stokes lines emanating from each turning point, defined by $\mathrm{Im}(\int_{x_t}^{x} S_{-1}\,\mathrm{d}x)=0$. Along a Stokes line, the WKB wave functions exhibit purely exponential behaviour without phase variation. The relative dominance between the two eigenfunctions is determined by the sign of $\mathrm{Re}(\int_{x_t}^{x} S_{-1}\,\mathrm{d}x)$. We use outward (inward) arrows to indicate the '+' ('–') eigenmode dominance. (iii) Introducing branch cuts to partition the Riemann surface into sheets mapped bijectively to the $\mathbb{C}$ plane.

3.2. *Exact WKB eigenfunctions*

The solution of (2.3) can be expressed as a linear combination of exact WKB eigenfunctions $\phi^{\pm}$, i.e. $\phi(x)=c^{+}\phi^{+}(x)+c^{-}\phi^{-}(x)$, where $c^{\pm}$ are constant coefficients.

In the vicinity of a simple regular turning point satisfying $\partial_x Q(x_t)\neq 0$, the original ODE can be mapped to the canonical Airy equation $\delta^2\partial_z^2\psi(z)-z\psi(z)=0$ via a local coordinate transformation $z(x)$ expanded as $z(x)\equiv\sum_{n,m}\delta^n z_{n,m}\Delta x^m$, where $\Delta x\equiv x-x_t$. The practical steps for computing the expansion coefficients $z_{n,m}$ are given by Kawai & Takei (2005, Chapter 2.3). The exact WKB eigenfunctions in this region are

$$\phi^{\pm}=\psi^{\pm}(\mathcal{L}^{-1}\mathcal{B}[z(x)]). \tag{3.4}$$

Away from the turning point, the eigenfunctions take the form

$$\phi^{\pm}=\psi^{\pm}\left(\mathcal{L}^{-1}\mathcal{B}[z(x_0)]\right)\exp\left(\int_{x_0}^{x}\mathcal{L}^{-1}\mathcal{B}[S^{\pm}]\,\mathrm{d}x\right), \tag{3.5}$$

where x_0 is a reference point chosen sufficiently far away from the turning point that both the Padé approximation of the Borel-resummed quantity $\mathcal{B}[S^{\pm}]$ and Taylor expansion of $z(x)$ in Δx remain valid.

3.3. *Connection formula*

The solution path, i.e. the daughter-wave trajectory defined on the complex $\mathbb{C}$ plane, is typically taken along the real axis. We denote its initial and final points by x_a and x_b, respectively.

Downloaded from https://www.cambridge.org/core. UNIVERSIDAD AUTONOMA METROPOLITANA, on 19 Nov 2026 at 15:26:59, subject to the Cambridge Core terms of use, available at https://www.cambridge.org/core/terms. https://doi.org/10.1017/S002237782610213X

In contrast to the conventional analytical approach, coefficients $c^{\pm}$ are constant only within each Stokes sector. Due to the discontinuous behaviour of the exact-WKB eigenfunctions across the Stokes lines, $c^{\pm}$ must undergo corresponding discontinuous jumps to ensure the continuity of the full solution $\phi(x)$.

The connection formula illustrates how the coefficients $c^{\pm}$ are transformed along the path. We denote by $c_a^{\pm}$ and $c_b^{\pm}$ the values of $c^{\pm}$ at the endpoints x_a and x_b, respectively. The connection formula is then expressed as

$$\begin{pmatrix} c_b^+ \\ c_b^- \end{pmatrix} = \boldsymbol{M}_j \cdots \boldsymbol{M}_2 \boldsymbol{M}_1 \begin{pmatrix} c_a^+ \\ c_a^- \end{pmatrix}. \tag{3.6}$$

The matrices $\boldsymbol{M}_{1\sim j}$ represent the transition matrices induced each time the solution path crosses the Stokes lines and branch cuts, encoding the jump of $c^{\pm}$. The explicit form of $\boldsymbol{M}$ depends on the local crossing geometry between the solution path and the lines. In particular, when the solution path crosses a Stokes line, the transition matrix is $\boldsymbol{M}_{\pm} = \begin{pmatrix} 1 & i \\ 0 & 1 \end{pmatrix}$ for Stokes lines where '+' eigenmode is dominant and $\begin{pmatrix} 1 & 0 \\ i & 1 \end{pmatrix}$ for Stokes lines where '–' eigenmode is dominant. By default, the wave path is taken counter-clockwise around the relevant turning point; for clockwise traversal, the corresponding transition matrix is $\boldsymbol{M}_{\pm}^{-1}$. Similarly, crossing a branch cut corresponds to the transition matrix $\boldsymbol{M}_c = \begin{pmatrix} 0 & -i \\ -i & 0 \end{pmatrix}$.

When a wave sequentially encounters Stokes lines from different turning points, a normalisation matrix must be applied before introducing the transition matrix of the subsequent turning point:

$$\boldsymbol{M}_V = \begin{pmatrix} \mathcal{L}^{-1}\mathcal{B}[e^{(1/2)\oint_I S^+ \mathrm{d}x}] & 0 \\ 0 & \mathcal{L}^{-1}\mathcal{B}\left[e^{(1/2)\oint_I S^- \mathrm{d}x}\right] \end{pmatrix}. \tag{3.7}$$

The total transition matrix is then given by $\boldsymbol{M}_V^{-1}\boldsymbol{M}\boldsymbol{M}_V$, with $\boldsymbol{M}$ in $\boldsymbol{M}_{\pm}$, $\boldsymbol{M}_c$. This matrix ensures the consistency of the global connection procedure. The Voros multiplier $V \equiv (1/2)\oint_I (S^+ - S^-)\,\mathrm{d}x$, with I denoting the closed contour encircling two associated turning points, is a key quantity for analysing wave coupling and potential well/barrier problems. Methods for calculating the Voros multiplier can be found elsewhere (Kreshchuk & Gulden 2019; Grassi, Hao & Neitzke 2022).

3.4. *Boundary condition of a daughter wave*

For convective PIs, one is often interested in how a pure incident daughter-wave perturbation at $x = x_a$ nonlinearly grows to a significant amplitude when it reaches a probe point $x = x_b$. In conventional WKB, one might set initial conditions such as $\phi(x_a) = c_a$, $\phi'(x_a) = c_a S_{-1}^+(x_a)/\delta$ to represent a pure incident '+' eigenmode. However, this introduces WKB approximation errors, generating a small admixture of the '–' eigenmode that might grow exponentially and obscure the '+' eigenmode of interest.

In the exact WKB framework, a pure incident daughter wave can be represented without admixture by

$$\phi(x_a) = c_a^+,\ \phi'(x_a) = c_a^+ \mathcal{L}^{-1}\mathcal{B}[S^+(x_a)]. \tag{3.8}$$

Downloaded from https://www.cambridge.org/core. UNIVERSIDAD AUTONOMA METROPOLITANA, on 19 Nov 2026 at 15:26:59, subject to the Cambridge Core terms of use, available at https://www.cambridge.org/core/terms. https://doi.org/10.1017/S002237782610213X

During the nonlinear coupling, mode exchange can occur: a daughter wave corresponding to '+' eigenmode at x_a may become a '–' eigenfunction at x_b, or *vice versa*. Considering this scenario, the amplification factor of this daughter wave is

$$A_{\text{inhom}} = \ln \frac{|c_b^- \phi^-(x_b)|}{|c_a^+ \phi^+(x_a)|} = \ln \frac{|c_b^-|}{|c_a^+|} + \ln \frac{|\phi^-(x_b)|}{|\phi^+(x_a)|}, \tag{3.9}$$

with the contributions from both the Stokes jump of constant coefficients and the amplitude difference of the eigenmodes at the endpoints, given by the two terms on the right-hand side of (3.9), respectively.

4. Exact WKB revisit of parametric instability in inhomogeneous plasmas

For the exact WKB analysis, we perform the transformation ϕ_1 to $\psi_1 \exp(-(1/2\epsilon)\int^x (K_0 - K_u - x)\mathrm{d}x)$, which reduces the system to the one-dimensional Schrödinger-type equation

$$\epsilon^2 \psi_1'' - \left[\frac{|\Gamma|^2}{v_{gu} v_{g1}} + \frac{i\epsilon}{2} - \frac{1}{4}(x - K_u + K_0)^2 \right] \psi_1 = 0. \tag{4.1}$$

As indicated by (3.9), the PI amplification consists of the Stokes jumps of the coefficients and the intrinsic evolution of the eigenmodes. Accordingly, in the following, we present: figure 1, the Stokes diagrams identifying locations of Stokes jumps and the associated transition matrices; figure 2, the wavenumber evolutions clarifying the correspondence between the two daughter waves and the '±' eigenmodes; and figure 3, the amplitude evolution of eigenmodes. Results for different PI regimes are shown together for direct comparison, followed by a case-by-case analysis of the resulting daughter-wave behaviour in the subsections.

Since (4.1) can also reduce to a Weber-type equation, an alternative analytical approach is available in terms of the parabolic cylinder functions D_ν. The eigenfunctions of the original ODE (2.3) can then be written as

$$\phi_1^{[1]} = \mathrm{e}^{\int^x (i/2\epsilon)(x + K_u - K_0)\,\mathrm{d}x} D_\nu \left(\sqrt{\frac{i}{\epsilon}} (x - K_u + K_0) \right),$$

$$\phi_1^{[2]} = \mathrm{e}^{\int^x (i/2\epsilon)(x + K_u - K_0)\,\mathrm{d}x} D_{-\nu-1} \left(\sqrt{\frac{-i}{\epsilon}} (x - K_u + K_0) \right), \tag{4.2}$$

where $\nu = ((i|\Gamma|^2)/\epsilon v_{gu} v_{g1}) - 1$. These analytical solutions, together with direct numerical solutions, will be used as mutual consistency checks for the exact WKB solutions developed in this work.

All figures are generated using the following parameter settings. The common parameters are $K_{ur} \equiv \mathrm{Re}(K_u) = 1.5$, $K_0 = 0.5$. The inhomogeneity ϵ is chosen as 0.1, a value that exceeds the conventional WKB limit established in our previous work. For non-resonant PI, the 'u' mode is strongly damped, which is modelled by setting $K_{ui} \equiv \mathrm{Im}(K_u) = \pm 2.0$, with the sign chosen such that damping occurs along the propagation direction: $K_{ui} > 0$ for forward scattering and $K_{ui} < 0$ for backward scattering. For resonant PI, $K_{ui} = 0$. The coupling strength is chosen as $(|\Gamma|^2)/v_{gu} v_{g1} = 0.25$ for forward scattering and –0.25 for backward scattering.

Figure 1 clearly shows how the wave path intersects the Stokes lines, where Stokes jumps occur. These intersection points are labelled as red P_j. The Stokes diagrams

Downloaded from https://www.cambridge.org/core. UNIVERSIDAD AUTONOMA METROPOLITANA, on 19 Nov 2026 at 15:26:59, subject to the Cambridge Core terms of use, available at https://www.cambridge.org/core/terms. https://doi.org/10.1017/S002237782610213X

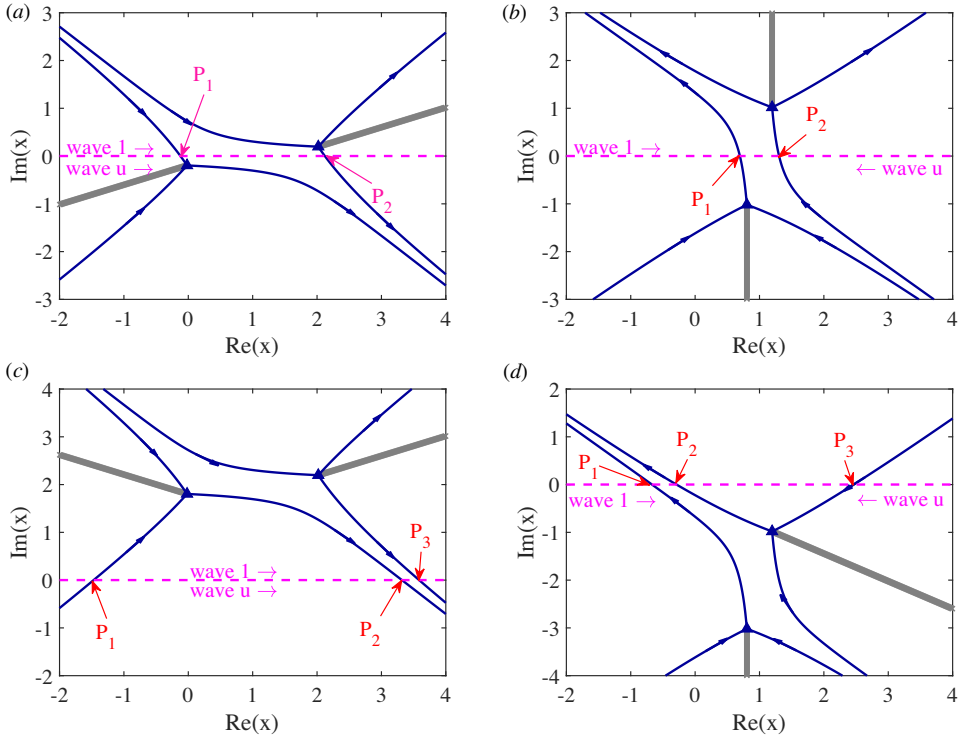


FIGURE 1. Stokes diagrams for PI regimes: (*a*) resonant forward scattering; (*b*) resonant backward scattering; (*c*) non-resonant forward scattering; (*d*) non-resonant backward scattering. Turning points are marked by triangles and branch cuts are represented by grey crosses. Solid blue lines are the Stokes lines, with arrows indicating the dominance of the '+' or '−' eigenmodes. The wave trajectory is noted by the pink dashed line. The propagating direction of each daughter wave is indicated by labelled arrows. The points P_j label the locations of Stokes jumps.

qualitatively reflect the distinct characteristics of different PI regimes. In the resonant forward scattering regime, the Stokes jump point lies close to the turning point, resulting in a well-localised and finite coupling region. By contrast, in the resonant backward scattering regime, the propagation path crosses the Stokes line nearly perpendicularly, so that no definite amplification or attenuation of the eigenmodes occurs along the real axis. As the system transitions from the resonant to the non-resonant regime, i.e. from figures 1(*a*,*b*) to figures 1(*c*,*d*), the increase of K_{ui} causes the Stokes jump points to move outward. Consequently, the coupling region becomes broader and less localised, and the growth is no longer confined to a specific interval.

These Stokes diagrams also exhibit several universal features. From (4.1), the two turning points are located at

$$x_t = K_u - K_0 \pm 2\sqrt{\frac{|\Gamma|^2}{v_{gu}v_{g1}} + \frac{i\epsilon}{2}}. \tag{4.3}$$

It follows that the separation between the turning points is independent of the PI regime, i.e. it is unaffected by variations in K_{ui}. Accordingly, the Stokes diagrams for different regimes are essentially equivalent up to global transformations. A variation

Downloaded from https://www.cambridge.org/core. UNIVERSIDAD AUTONOMA METROPOLITANA, on 19 Nov 2026 at 15:26:59, subject to the Cambridge Core terms of use, available at https://www.cambridge.org/core/terms. https://doi.org/10.1017/S002237782610213X

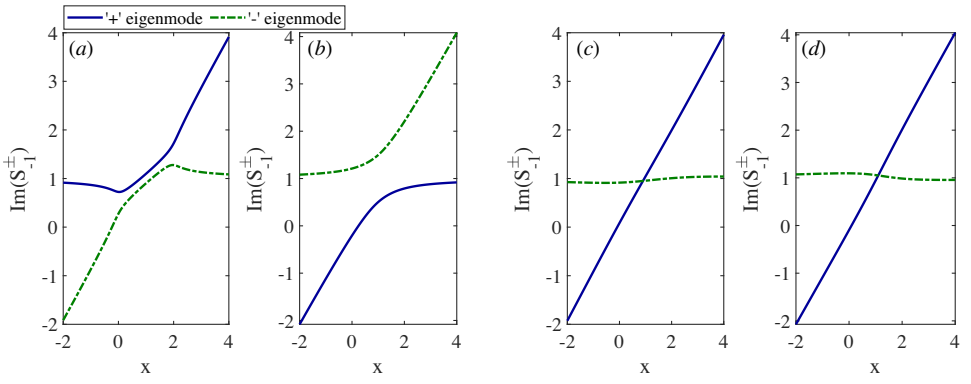


FIGURE 2. Eigenmode wavenumbers along the wave trajectory for PI regimes: (*a*) resonant forward scattering; (*b*) resonant backward scattering; (*c*) non-resonant forward scattering; (*d*) non-resonant backward scattering. These figures allow identification of which eigenmode corresponds to each daughter wave as $x \to \pm\infty$.

in K_{ui} results in a vertical translation of the diagram, corresponding to the transition between resonant and non-resonant regimes. A sign change of $v_{gu}v_{g1}$ induces a 90° rotation of the diagram, corresponding to the transition between forward and backward scattering.

In all cases, the distance between the turning points remains invariant, as does the Voros multiplier associated with the turning-point pair. It is given by

$$V = \frac{1}{2}\oint_I \sqrt{Q(x)}\,\mathrm{d}x = \pi\left(\frac{|\Gamma|^2}{v_{gu}v_{g1}} + i\epsilon\right), \tag{4.4}$$

and its real part $V_r \equiv \mathrm{Re}(V)$ coincides exactly with the common amplification factor obtained from the conventional WKB result in (2.5).

The linear wavenumber of the daughter wave '1' varies linearly as $K_1 = \epsilon x$, whereas that of the daughter wave 'u' remains constant $K_u - K_0$. As shown in figure 2(*a,b*), mode exchange occurs: for instance, in figure 2(*a*), the '+' eigenmode behaves as the '*u*' wave in the limit $x \to -\infty$, while it evolves into the '1' wave as $x \to +\infty$. This exchange indicates the presence of strong Stokes jumps in the resonant PI regime. By contrast, figure 2(*c,d*) shows no mode exchange, suggesting that the associated Stokes jumps are weak for non-resonant regimes.

Eigenmode evolution of resonant forward scattering in figure 3(*a*) differs from resonant backward scattering in figure 3(*b*). In the coupling region defined by the interval between the jump positions noted by red dashed lines, the eigenmodes in the resonant forward scattering regime vary quickly. In contrast, those in the resonant backward scattering merely change. For the non-resonant regimes in figures 3(*c,d*), the wave '1' slowly varies, while the quasi-mode '*u*' linearly damps.

Now, we discuss the four different PI regimes one by one.

4.1. *Resonant forward scattering*

In the resonant forward scattering regime, both daughter waves '1' and '*u*' are resonant and propagate from $-\infty$ to $+\infty$. As shown in figure 2(*a*), wave '1' corresponds to eigenmode '–' at $x \to -\infty$ and '+' at '$x \to +\infty$', while wave '*u*' behaves

Downloaded from https://www.cambridge.org/core. UNIVERSIDAD AUTONOMA METROPOLITANA, on 19 Nov 2026 at 15:26:59, subject to the Cambridge Core terms of use, available at https://www.cambridge.org/core/terms. https://doi.org/10.1017/S002237782610213X

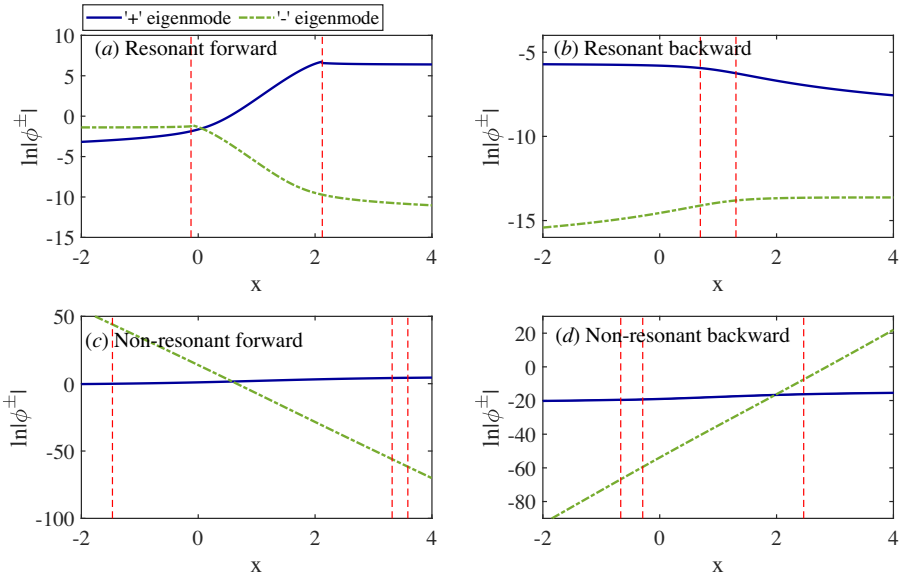


FIGURE 3. Eigenmode amplitude evolution along the wave trajectory. Red dashed vertical lines indicate the locations of Stokes jumps. Each panel corresponds to a PI regime, as in figures 1 and 2. The coupling region is defined as the interval between the first and last Stokes jumps.

inversely. Assuming the coefficients $c_a^{\pm}$ before coupling are known, the coefficients $c_b^{\mp}$ after coupling can be determined by the connection formula.

According to the Stokes diagram in figure 1(*a*), the wave encounters two Stokes lines and the connection formula is

$$\begin{pmatrix} c_b^+ \\ c_b^- \end{pmatrix} = \begin{pmatrix} 1 & 0 \\ ie^{2V/\epsilon} & 1 \end{pmatrix} \begin{pmatrix} 1 & -i \\ 0 & 1 \end{pmatrix} \begin{pmatrix} c_a^+ \\ c_a^- \end{pmatrix}. \tag{4.5}$$

Consequently, for wave '1', the Stokes jump yields

$$c_a^- \to c_b^+ = c_a^+ - ic_a^-. \tag{4.6}$$

However, for wave '*u*', the jump result yields

$$c_a^+ \to c_b^- = ic_a^+ e^{2V/\epsilon} + c_a^- \left(1 + e^{2V/\epsilon}\right). \tag{4.7}$$

The final amplitude of one daughter wave depends not only on its incident amplitude, but also on that of the other daughter wave. Since daughter waves are typically seeded by background noise, arbitrary initial conditions $c_a^{\pm}$ may in principle be realised. Special cases, such as $c_a^+ = ic_a^-$, which lead to the vanishing of wave '1' after coupling, are also possible. However, our physical interest usually lies in the strongly amplified daughter waves that grow from the noise floor to amplitudes large enough to affect the system dynamics. Since this requires amplification over many orders of magnitude, the relevant regime is typically of large amplification ($A \gg 1$). In this limit, even a modest difference in amplification factor is exponentially magnified, such that the seed corresponding to the maximum amplification overwhelmingly dominates the final wave amplitude. Therefore, for most practical purposes, such as

Downloaded from https://www.cambridge.org/core. UNIVERSIDAD AUTONOMA METROPOLITANA, on 19 Nov 2026 at 15:26:59, subject to the Cambridge Core terms of use, available at https://www.cambridge.org/core/terms. https://doi.org/10.1017/S002237782610213X

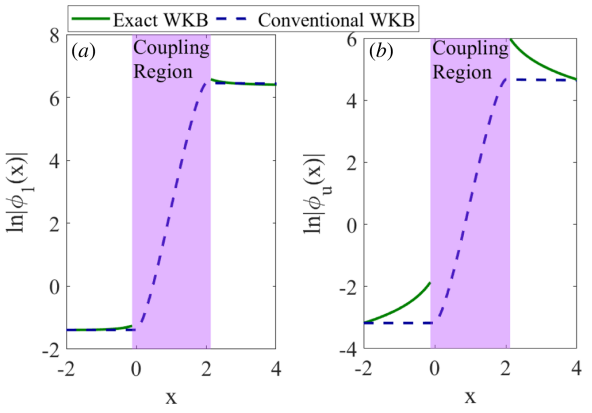


FIGURE 4. Amplitude evolution of (a) daughter wave 'u' and (b) daughter wave '1' for resonant forward scattering PI. From the exact WKB perspective, the green solid lines represent waves with well-defined wavenumbers, while purple-shaded regions indicate intervals where the daughter waves are strongly coupled and cannot be clearly distinguished. The blue dashed lines show the amplitude evolution predicted by the conventional WKB method. The incident coefficients are $c_a^+ = 1$, $c_a^- = 0$ for panel (a) and $c_a^+ = 0$, $c_a^- = 1$ for panel (b).

evaluating the PI-induced lower hybrid sidebands in tokamaks (Cesario *et al.* 2004) or estimating the worst gain induced by stimulated Raman scattering in inertial confinement fusion (Rosenberg *et al.* 2018), it is sufficient to consider only the boundary condition that yields the maximum amplification.

In figure 4, the actual wave amplitude evolution is traced by combining the eigenmode evolution with the Stokes jumps. When focusing on the evolution of a single wave, the incident coefficient of the other daughter wave is set to zero. It can be observed that, although the final amplification predicted by the exact WKB and the conventional WKB approaches is identical, the local wave behaviours exhibit clear differences near the boundaries of the coupling region, i.e. in the vicinity of the turning points. In this region, higher-order WKB corrections become significant and the conventional WKB validity condition breaks down. Remarkably, the higher-order contributions from the two turning points cancel each other, which ultimately leads to the same prediction for the final amplification factor.

Consistency checks of the exact WKB solutions of the original ODE (2.3) are presented in figure 5, where they are found to be in indistinguishable agreement with numerical solutions and the parabolic cylinder representation.

4.2. *Resonant backward scattering*

In the resonant backward scattering regime, wave 'u' propagates in the opposite direction. From the wave-vector evolution shown in figure 2(b), we identify that the '+' eigenmode at $x \to -\infty$ and the '–' eigenmode $x \to +\infty$ correspond to wave '1', whereas the '–' eigenmode at $x \to -\infty$ and '+' eigenmode at $x \to +\infty$ correspond to wave 'u'. Therefore, the two coefficients representing the incident waves are c_a^+ and c_b^+. Indicated by the Stokes diagram in figure 1(b), the connection formula is

$$\begin{pmatrix} c_b^+ \\ c_b^- \end{pmatrix} = \begin{pmatrix} 1 & ie^{2V/\epsilon} \\ 0 & 1 \end{pmatrix} \begin{pmatrix} 1 & 0 \\ -i & 1 \end{pmatrix} \begin{pmatrix} c_a^+ \\ c_a^- \end{pmatrix}. \tag{4.8}$$

Downloaded from https://www.cambridge.org/core. UNIVERSIDAD AUTONOMA METROPOLITANA, on 19 Nov 2026 at 15:26:59, subject to the Cambridge Core terms of use, available at https://www.cambridge.org/core/terms. https://doi.org/10.1017/S002237782610213X

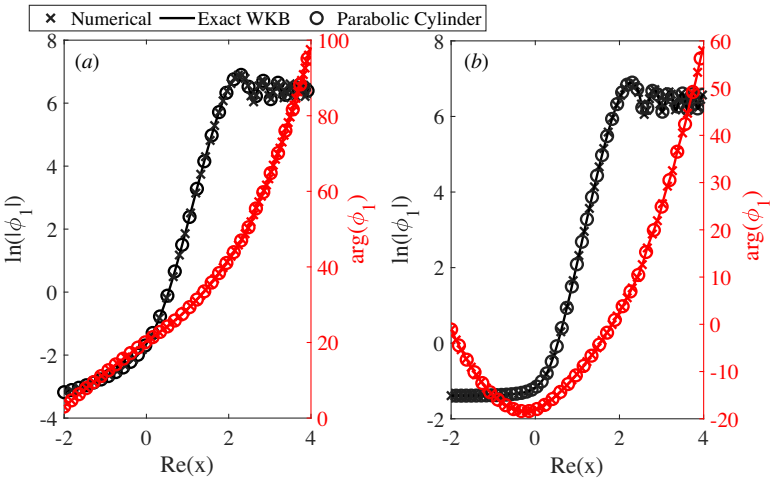


FIGURE 5. The ϕ_1 solution of (2.3) obtained via exact WKB (solid line), a numerical ODE solver (crosses) and the parabolic cylinder function representation in (4.2) (circles) for the resonant forward scattering regime. Black curves/markers denote the amplitude of ϕ_1, while red curves/markers denote the unwrapped phase. Parameters of panels (*a*) and (*b*) are the same as those used in figures 4(*a*) and 4(*b*), respectively.

For wave '1', the Stokes jump is

$$c_a^+ \to c_b^- = ie^{-2V/\epsilon}(c_a^+ - c_b^+), \tag{4.9}$$

while for wave '*u*', which propagates in the opposite direction to wave '1', the Stokes jump reads

$$c_b^+ \to c_a^- = ie^{-2V/\epsilon}(c_a^+ - c_b^+) + ic_a^+. \tag{4.10}$$

Note that in backward-scattering regimes, $V_r < 0$ because $v_{gu}v_{g1} < 0$. Since we are only interested in the maximally amplified PI response, we focus on cases in which the large factor $\exp(2|V_r|/\epsilon)$ appears in the post-coupling coefficients c_a^- and c_b^-. Combinations such as $c_a^+ = c_b^+$ are therefore disregarded.

The amplitudes of the $\pm$ eigenmodes shown in figure 3(*b*) vary little across space, yet the amplitude difference between the '+' and '–' eigenmodes becomes pronounced. This disparity arises from the $\mathcal{L}^{-1}\mathcal{B}[S^+]$ integral evaluated from the upper turning point in figure 1(*b*) to 0, together with the $\mathcal{S}[R^-]$ integral from the lower turning point to 0. These two contribute to an amplitude disparity approximately $|\phi_-/\phi_+| \simeq \exp(-|V_r|/\epsilon)$.

Taking into account that the Stokes jump already provides an amplification of $\exp(-2V_r/\epsilon)$, the final amplification factors of both daughter waves are estimated as $\exp(-V_r/\epsilon)$. To confirm this precisely, figure 6 shows the amplitude evolution from the perspective of exact WKB. Again, when examining the growth of a particular daughter wave, the incident coefficient of the other wave is set to 0. The logarithmic amplitude difference between ends of the interval results in 7.854 for both daughter waves, consistent with the estimated amplification factor $A_{\text{inhom}} = |V_r|/\epsilon$, identical to the resonant forward scattering case. Verification of the exact WKB solution for this regime is shown in figure 7, demonstrating full consistency among all methods.

Downloaded from https://www.cambridge.org/core. UNIVERSIDAD AUTONOMA METROPOLITANA, on 19 Nov 2026 at 15:26:59, subject to the Cambridge Core terms of use, available at https://www.cambridge.org/core/terms. https://doi.org/10.1017/S002237782610213X

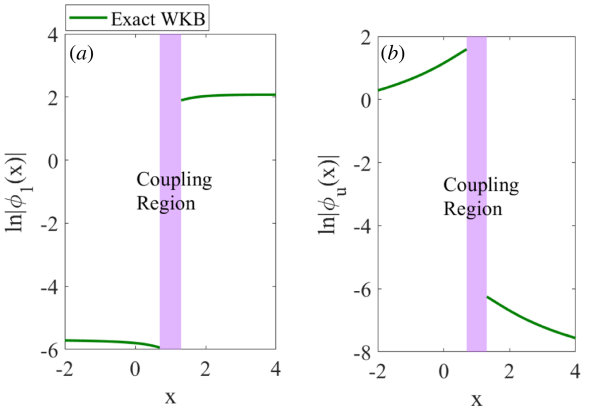


FIGURE 6. Amplitude evolution of (a) wave '1' and (b) wave 'u' in resonant backward scattering PI. The purple shaded regions represent coupling intervals where the two daughter waves cannot be distinguished from each other. The incident coefficients are chosen as $c_a^+ = 1$, $c_b^+ = 0$ in panel (a) and $c_a^+ = 0$, $c_b^+ = 1$ in panel (b).

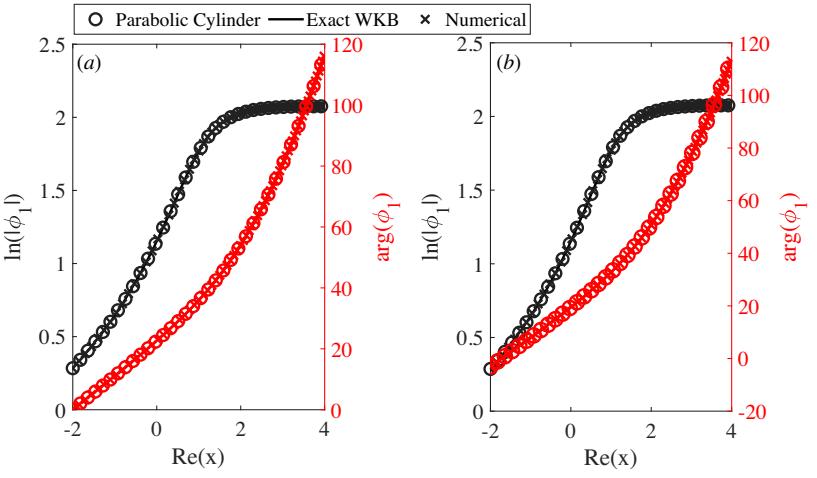


FIGURE 7. Comparison of the solution ϕ_1 of (2.3) obtained from the exact-WKB method (solid lines), a numerical ODE solver (crosses) and the parabolic-cylinder-function representation (4.2) (circles) for the resonant backward scattering regime. Black curves/markers denote the amplitude of ϕ_1, and red curves/markers denote the unwrapped phase. Panels (a) and (b) use the same parameters as figures 6(a) and 6(b), respectively.

The $\exp(|V_r|/\epsilon)$ amplification appears to contradict the zero amplification predicted by (2.5). From the conventional WKB perspective, the zero amplification results from the fact that none of the phase integrands $\pm\sqrt{Q(x)}$ on the entire real axis possesses a real part, except for small corrections of order $O(\epsilon)$.

The discrepancy originates from an intrinsic limitation of the conventional WKB method, which ignores Stokes jumps. This ignorance of Stokes jumps is equivalent to an implicit boundary condition that the amplitude of the unconcerned wave vanishes at the incident side of the concerned wave; only then can the eigenmode

Downloaded from https://www.cambridge.org/core. UNIVERSIDAD AUTONOMA METROPOLITANA, on 19 Nov 2026 at 15:26:59, subject to the Cambridge Core terms of use, available at https://www.cambridge.org/core/terms. https://doi.org/10.1017/S002237782610213X

corresponding to the incident concerned wave evolve without a coefficient jump. In the resonant forward scattering regime, where both daughter waves propagate in the same direction, this assumption causes no issue. However, in the resonant backward scattering regime, it effectively sets the outgoing amplitude of the counter-propagating wave '*u*' to zero. Since parametric amplification relies on a positive-feedback loop between both waves, suppressing one prevents the growth of the other, leading to the zero amplification predicted by conventional WKB. This can be verified by substituting $c_a^- = 0$ into (4.9) and (4.10), which yields $c_b^- = -ic_a^+$ and a final attenuation of wave '1' about $\exp(-|V_r|/\epsilon)$.

As shown within the exact WKB framework, the zero amplification predicted by the conventional WKB treatment for resonant backward scattering PIs ($(\Gamma\Gamma^*/v_{gu}v_{g1}) < 0$) is invalid, due to the omission of boundary-condition data, in particular, Stokes jumps. In our previous work (Zhou *et al.* 2025), the condition $\alpha\alpha^* < 0$ was expressed in terms of $\alpha = \Gamma/v_{gu}$ and $\alpha^* = \Gamma^*/v_{g1}$ without distinguishing whether it arises from $\Gamma\Gamma^* > 0$, $v_{gu}v_{g1} < 0$ or $\Gamma\Gamma^* < 0$, $v_{gu}v_{g1} > 0$ (in the latter case, Γ^* is no longer the complex conjugate of Γ). The present analysis shows that these cases lead to fundamentally different behaviours. The former, i.e. the resonant backward scattering considered here, yields finite amplification, whereas the latter corresponds to the resonant forward scattering with zero amplification. Nevertheless, the previously reported mechanism, whereby increasing the linear growth rate of the daughter wave '*u*' in the latter regime breaks the negative feedback loop and restores PI amplification, remains applicable.

4.3. *Non-resonant forward scattering*

Compared with the resonant type, where the incident amplitudes of both daughter waves must be prescribed, the non-resonant regime allows a much simpler boundary condition, as the heavily damping quasi-mode cannot exist as an incident wave and is instead generated exclusively through nonlinear coupling.

Figure 2(*c*) shows that the '+' eigenmode corresponds to daughter wave '1' and the '–' eigenmode corresponds to the quasi-mode '*u*' throughout the domain, without any mode exchange as in the resonant regimes.

Given that the quasi-mode's incident coefficient c_a^- is zero and Stokes diagram in figure 1(*c*), we have the connection formula:

$$\begin{pmatrix} c_b^+ \\ c_b^- \end{pmatrix} = \begin{pmatrix} 1 & 0 \\ ie^{2V/\epsilon} & 1 \end{pmatrix} \begin{pmatrix} 1 & 0 \\ i & 1 \end{pmatrix} \begin{pmatrix} 1 & i \\ 0 & 1 \end{pmatrix} \begin{pmatrix} c_a^+ \\ 0 \end{pmatrix}. \tag{4.11}$$

Solving the connection formula, we find that the Stokes jump for wave '1' is

$$c_a^+ \to c_b^+ = c_a^+, \tag{4.12}$$

while the quasi-mode's Stokes jump yields

$$c_a^- = 0 \to c_b^- = ic_a^+ \left(1 + e^{2V/\epsilon}\right). \tag{4.13}$$

Therefore, amplification of wave '1' does not depend on the Stokes jump and is entirely governed by its intrinsic spatial evolution, as illustrated in figure 8(*a*). Because of the absence of Stokes jump contribution and mode exchange, the conventional WKB treatment remains valid in this regime.

In the conventional WKB approach, increasing the linear spatial damping rate K_{ui} of quasi-mode '*u*' causes the effective growth rate to spread across the entire

Downloaded from https://www.cambridge.org/core. UNIVERSIDAD AUTONOMA METROPOLITANA, on 19 Nov 2026 at 15:26:59, subject to the Cambridge Core terms of use, available at https://www.cambridge.org/core/terms. https://doi.org/10.1017/S002237782610213X

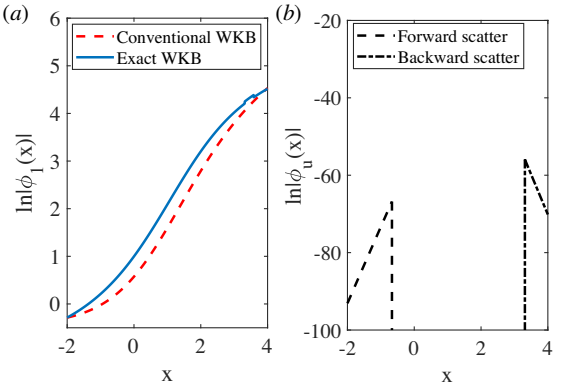


FIGURE 8. Amplitude evolution of (*a*) wave '1' and (*b*) quasi-mode '*u*' for non-resonant parametric instability (PI) within the exact WKB framework. The behaviour of wave '1' in panel (*a*) is identical for forward and backward scattering; thus, only one case is shown. The conventional WKB result is included as a blue solid line for comparison. In panel (*b*), the quasi-mode '*u*' exists only over part of the spatial interval, as it is generated solely through nonlinear coupling.

real axis, rather than remaining localised between the turning points. Consequently, the integral evaluated over a finite region becomes smaller than the standard value V_r/ϵ.

We also compare the conventional WKB prediction with the evolution obtained from the exact WKB analysis in figure 8(*a*). The final amplification factor of daughter wave '1' between a fixed spatial interval is found to be identical in both approaches. Although the higher-order WKB terms included in the exact WKB framework modify the local amplitude, these contributions are axially symmetric about the midpoint between the two turning points, and thus their net contribution to the integral over the entire interval vanishes.

The evolution of the quasi-mode is shown in figure 8(*b*). It is triggered by a Stokes jump at the second crossing point, with an amplitude much smaller than wave '1', and quickly decays due to strong linear damping. This may account for the difficulty in experimentally detecting the quasi-mode. Figure 9(*a*) compares exact WKB solutions in this regime with other methods, showing that the results of all the approaches are numerically distinguishable.

4.4. *Non-resonant backward scattering*

Finally, the results in the non-resonant backward scattering case are nearly identical to those of the non-resonant forward scattering case. The key difference is that the quasi-mode '*u*' propagates and damps in the negative x-direction, leading to the boundary condition $c_b^- = 0$.

The connection formula based on Stokes diagram in figure 1(*d*) is

$$\begin{pmatrix} c_b^+ \\ 0 \end{pmatrix} = \begin{pmatrix} 1 & -ie^{2V/\epsilon} \\ 0 & 1 \end{pmatrix} \begin{pmatrix} 1 & 0 \\ -ie^{-2V/\epsilon} & 1 \end{pmatrix} \begin{pmatrix} 1 & 0 \\ -i & 1 \end{pmatrix} \begin{pmatrix} c_a^+ \\ c_a^- \end{pmatrix}. \tag{4.14}$$

The Stokes jump of wave '1' is the same as (4.12), indicating no contribution to PI amplification. The Stokes jump of quasi-mode '*u*' is given by

$$c_b^- = 0 \to c_a^- = ic_a^+(1 + e^{-2V/\epsilon}). \tag{4.15}$$

Downloaded from https://www.cambridge.org/core. UNIVERSIDAD AUTONOMA METROPOLITANA, on 19 Nov 2026 at 15:26:59, subject to the Cambridge Core terms of use, available at https://www.cambridge.org/core/terms. https://doi.org/10.1017/S002237782610213X

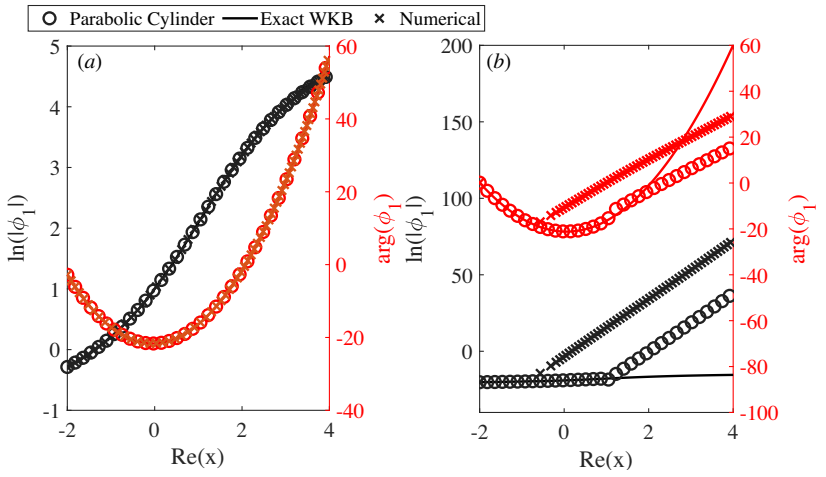


FIGURE 9. Comparison of the solution ϕ_1 of (2.3) obtained from the exact-WKB method (solid lines), a numerical ODE solver (crosses) and the parabolic-cylinder-function representation in (4.2) (circles). Panel (*a*) is the non-resonant forward scattering PI regime, while panel (*b*) is the non-resonant backward scattering. Black curves/markers denote the amplitude of ϕ_1 and red curves/markers denote the unwrapped phase. The linear growth trend observed in the parabolic cylinder representation and numerical solution in panel (*b*) indicates the onset of numerical stability.

The intrinsic amplitude evolution of wave '1' is the same as in the non-resonant forward regime shown in figure 8(*a*). As shown in figure 8(*b*), the quasi-mode '*u*' is generated at the crossing point P_2 in figure 1(*d*), with again an amplitude that remains negligibly small and rapidly decays due to linear damping.

Cross-validation for this regime is presented in figure 9(*b*). The numerical solution becomes unstable beyond $\mathrm{Re}(x) = -0.74$, as the quasi-mode exponentially amplifies the small numerical errors during propagation toward increasing x. The analytical solution based on parabolic cylinder functions also breaks down beyond $\mathrm{Re}(x) = 1.08$, where severe cancellation occurs between the two large contributions satisfying $c^{[1]}\phi_1^{[1]} \simeq -c^{[2]}\phi_1^{[2]}$. In contrast, the exact WKB solution remains stable throughout the entire domain, maintaining a well-behaved amplitude and phase without any sign of breakdown. This demonstrates the superior robustness of the exact WKB approach compared with both direct numerical integration and analytical representations via special functions.

5. Conclusions and discussions

In this work, the exact WKB method is employed to examine the coupled daughter-wave equations governing various types of convective parametric instability (PI) in inhomogeneous plasmas, including both resonant and non-resonant regimes as well as forward scattering and backward scattering regimes. While this problem has been previously studied by Zhou *et al.* (2025) within the conventional WKB framework, we revisit it here using the exact WKB approach to overcome several limitations inherent in the conventional WKB treatment.

Compared with the conventional WKB approach, the exact WKB method offers two key advantages. First, it is not restricted by the WKB validity conditions and can be systematically applied to ODEs with spatially varying coefficients at arbitrary

Downloaded from https://www.cambridge.org/core. UNIVERSIDAD AUTONOMA METROPOLITANA, on 19 Nov 2026 at 15:26:59, subject to the Cambridge Core terms of use, available at https://www.cambridge.org/core/terms. https://doi.org/10.1017/S002237782610213X

order. Second, it naturally incorporates the boundary conditions, whereas conventional WKB typically tracks only the integral of a single eigenvalue, thus failing to capture the effects of Stokes jumps.

From the exact WKB perspective, the amplification of the daughter waves arises from two mechanisms: the Stokes jumps and the intrinsic spatial evolution of the eigenmodes. As a result, the amplification factor of all four types of PI is found to be

$$A_{\mathrm{inhom}} = |V_r|/\epsilon = \frac{\pi|\Gamma|^2}{\epsilon|v_{gu}v_{g1}|}, \tag{5.1}$$

where it depends on the coupling coefficient Γ, the group velocities v_g of the daughter waves and the strength of inhomogeneity ϵ. The term V_r originates from the real part of the Voros multiplier, namely the contour integral around the turning points. Variations in the PI regime merely induce global translations or rotations of the Stokes diagram and therefore do not affect the value of V_r.

As a complementary remark, we briefly comment on certain resonant PI regimes that lie outside the noise-seeded large-amplification regime primarily considered in this work. In these cases, the amplification remains small, and both daughter-wave incident amplitudes are explicitly specified. The amplification factor then becomes additionally dependent on the initial amplitude ratio. Using the Stokes jump relations in (4.6) and (4.9), as well as their eigenfunction evolution shown in figure 3(*a*,*b*), the amplification factor is corrected as $|V_r|/\epsilon + \ln|c_1 - ic_u| - \ln|c_1|$, where c_1 and c_u are initial coefficients of wave '1' and 'u', respectively.

Results previously obtained using the conventional WKB approach are also corrected by the exact WKB method. Owing to its inability to account for Stokes jumps, the conventional WKB treatment predicts zero amplification for resonant backward scattering PI, as indicated by (2.5). In contrast, the exact WKB analysis shows that Stokes jumps dominate the amplification in this regime, yielding an amplification factor $|V_r|/\epsilon$.

It is noteworthy that the present study primarily serves as an initial demonstration of the applicability of the exact WKB method to the analysis of PIs. More complex scenarios, such as the influence of daughter-wave reflection or mode conversion on the PI process governed by a third-order ODE or higher, can in principle be treated within the exact WKB framework, but are not considered in the present revisit and will be addressed in future work.

While such more complex scenarios are not included in the present analysis, the effect of strong plasma inhomogeneity for PIs described by (2.1) and (2.2) can already be examined within the current framework. As long as the governing ODE can be reduced to a Weber equation like (4.1), its amplification factor is universally inversely proportional to the parameter gradient ϵ, regardless of the value of ϵ. The Voros multiplier V is independent of ϵ because the net contribution of the higher-order WKB terms vanishes, yielding

$$V = \frac{\epsilon}{2}\oint_I \mathcal{L}^{-1}\mathcal{B}[S^+ - S^-]\mathrm{d}x = \frac{1}{2}\oint_I (S^+_{-1} - S^-_{-1})\mathrm{d}x. \tag{5.2}$$

For more complex systems, such as higher-order ODEs or Schrödinger-type equations with polynomial potentials $Q(x)$ containing quartic terms, the associated Picard–Fuchs equation for V generally has differential order higher than one. In such cases, the Voros multiplier exhibits a non-trivial dependence on the

Downloaded from https://www.cambridge.org/core. UNIVERSIDAD AUTONOMA METROPOLITANA, on 19 Nov 2026 at 15:26:59, subject to the Cambridge Core terms of use, available at https://www.cambridge.org/core/terms. https://doi.org/10.1017/S002237782610213X

inhomogeneity parameter ϵ. These more intricate scenarios will be systematically investigated within the exact WKB framework in future work.

Acknowledgements

Editor Louise Willingale thanks the referees for their advice in evaluating this article.

Funding

This work was supported by the Hundred Talents Program of the Chinese Academy of Science, the Strategic Priority Research Program of Chinese Academy of Sciences (Grant Nos. XDB0790000 and XDB0500302) and the National Natural Science Foundation of China (Grant Nos. 12375231 and 12575245).

Declaration of interests

The authors report no conflict of interest.

REFERENCES

AFEYAN, B.B. & WILLIAMS, E.A. 1995 Unified theory of stimulated raman scattering and two-plasmon decay in inhomogeneous plasmas: high frequency hybrid instability. *Phys. Rev. Lett.* **75**, 4218–4221.

BAHAR, E. 1967 Generalized WKB method with applications to problems of propagation in nonhomogeneous media. *J. Math. Phys.* **8**, 1735–1746.

BALIAN, R., PARISI, G. & VOROS, A. 1978 Discrepancies from asymptotic series and their relation to complex classical trajectories. *Phys. Rev. Lett.* **41**, 1141–1144.

BAO, J., LIN, Z., KULEY, A. & WANG, Z.X. 2016 Nonlinear electromagnetic formulation for particle-in-cell simulation of lower hybrid waves in toroidal geometry. *Phys. Plasmas* **23**, 062501.

CASTALDO, C. & NAPOLI, F. 2024 Nonlinear lower hybrid wave equations in collisional tokamak plasmas. *Plasma Phys. Control. Fusion* **66**, 095005.

CESARIO, R., CARDINALI, A., CASTALDO, C., PAOLETTI, F., FUNDAMENSKI, W., HACQUIN, S. & the JET-EFDA workprogramme contributors 2006 Spectral broadening of lower hybrid waves produced by parametric instability in current drive experiments of tokamak plasmas. *Nucl. Fusion* **46**, 462–476.

CESARIO, R., CARDINALI, A., CASTALDO, C., PAOLETTI, F. & MAZON, D. 2004 Modeling of a lower-hybrid current drive by including spectral broadening induced by parametric instability in tokamak plasmas. *Phys. Rev. Lett.* **92**, 175002.

CHEN, F.F. 1984 Introduction to plasma physics and controlled fusion. In *International Series of Monographs on Physics*, vol. 1. Plenum Press.

CHEN, K. & GAO, Z. 2025 Saturation of a quasi-mode parametric instability in an inhomogeneous plasma. *Nucl. Fusion* **65**, 036020.

CHEN, L. & BERGER, R.L. 1977 Spatial depletion of the lower hybrid cone through parametric decay. *Nucl. Fusion* **17**, 779–785.

CODESIDO, S. & MARIÑO, M. 2018 Holomorphic anomaly and quantum mechanics. *J. Phys. A: Math. Theor.* **51**, 055402.

DING, B.J. *et al.* 2018 Correlation between the onset of parametric instability of lower hybrid waves and modification in edge plasma current profile on EAST. *Nucl. Fusion* **58**, 126015.

DUBOIS, D.F., BEZZERIDES, B. & ROSE, H.A. 1992 Collective parametric instabilities of many overlapping laser beams with finite bandwidth. *Phys. Fluids B* **4**, 241–251.

DUNNE, G.V. & ÜNSAL, M. 2017 WKB and resurgence in the Mathieu equation. In *Resurgence, Physics and Numbers* (ed. Frédéric Fauvet, Dominique Manchon, Stefano Marmi & David Sauzin), pp. 249–298. Scuola Normale Superiore.

ENOMOTO, S. & MATSUDA, T. 2023 The exact WKB analysis for asymmetric scalar preheating. *J. High Energy Phys.* **2023**, 88.

FISCH, N.J. 1987 Theory of current drive in plasmas. *Rev. Mod. Phys.* **59**, 175–234.

Downloaded from https://www.cambridge.org/core. UNIVERSIDAD AUTONOMA METROPOLITANA, on 19 Nov 2026 at 15:26:59, subject to the Cambridge Core terms of use , available at https://www.cambridge.org/core/terms. https://doi.org/10.1017/S002237782610213X

FUJIMORI, T., KAMATA, S., MISUMI, T., SUEISHI, N. & TAYA, H. 2025 Exact Wentzel–Kramers–Brillouin (WKB) analysis of two-level floquet systems. *Prog. Theor. Exp. Phys.* **2025**, 103A02.

GRASSI, A., HAO, Q. & NEITZKE, A. 2022 Exact WKB methods in SU(2) Nf = 1. *J. High Energy Phys.* **2022**, 46.

HELLWARTH, R.W. 1963 Theory of stimulated Raman scattering. *Phys. Rev.* **130**, 1850–1852.

HONDA, N., KAWAI, T. & TAKEI, Y. 2015 Virtual turning points. In *SpringerBriefs in Mathematical Physics*, vol. 4. Springer Japan.

HUANG, Z.K., SU, Z.H., CHEN, K.Y., ZENG, L. & GAO, Z. 2026 PIPERS: a ray tracing program of RF waves coupled with parametric decay instabilities around the scrape-off layer. *Nucl. Fusion* **66**, 016022.

IMAIZUMI, K. 2020 Exact WKB analysis and TBA equations for the Mathieu equation. *Phys. Lett. B* **806**, 135500.

ITO, K., MARIÑO, M. & SHU, H. 2019 TBA equations and resurgent quantum mechanics. *J. High Energy Phys.* **2019**, 228.

ITO, K. & YANG, J. 2024 Exact WKB analysis and TBA equations for the stark effect. *Prog. Theor. Exp. Phys.* **2024**, 013A02.

IWAKI, K. 2024 Les Houches lectures on exact WKB method and Painlevé equations. *Tech. Rep.* University of Tokyo, Les Houches.

KAMATA, S., MISUMI, T., SUEISHI, N. & ÜNSAL, M. 2023 Exact WKB analysis for SUSY and quantum deformed potentials: quantum mechanics with Grassmann fields and Wess-Zumino terms. *Phys. Rev. D* **107**, 045019.

KAUP, D.J., REIMAN, A. & BERS, A. 1979 Space-time evolution of nonlinear three-wave interactions. I. Interaction in a homogeneous medium. *Rev. Mod. Phys.* **51**, 275–309.

KAWAI, T. & TAKEI, Y. 2005 Algebraic analysis of singular perturbation theory. In *Translations of Mathematical Monographs*, vol. 227. American Mathematical Society.

KONOPLYA, R.A., ZHIDENKO, A. & ZINHAILO, A.F. 2019 Higher order WKB formula for quasinormal modes and grey-body factors: recipes for quick and accurate calculations. *Classical Quant. Grav.* **36**, 155002.

KRESHCHUK, M. & GULDEN, T. 2019 The Picard–Fuchs equation in classical and quantum physics: application to higher-order WKB method. *J. Phys. A: Math. Theor.* **52**, 155301.

LI, G., ZHOU, T., LI, M., DING, B., GAN, C., YAN, N. & XIANG, N. 2024 The onset of parametric decay of lower hybrid waves during lower hybrid current drive experiments on Experimental Advanced Superconducting Tokamak. *Nucl. Fusion* **64**, 126008.

LIU, C.S. & TRIPATHI, V.K. 1985 Parametric instabilities in a magnetized plasma. *Phys. Rep.* **3**, 143–216.

LIU, C.S., TRIPATHI, V.K., CHAN, V.S. & STEFAN, V. 1984 Density threshold for parametric instability of lower-hybrid waves in tokamaks. *Phys. Fluids* **27**, 1709.

MA, H.H., LI, X.F., WENG, S.M., YEW, S.H., KAWATA, S., GIBBON, P., SHENG, Z.M. & ZHANG, J. 2021 Mitigating parametric instabilities in plasmas by sunlight-like lasers. *Matter Radiat. Extremes* **6**, 055902.

MIYACHI, T., NAMBA, R., OMIYA, H. & OSHITA, N. 2025 Path to an exact WKB analysis of black hole quasinormal modes. *Phys. Rev. D* **111**, 124045.

NAPOLI, F., CASTALDO, C., CESARIO, R. & SCHETTINI, G. 2013 Modeling of the nonlinear mode coupling of lower hybrid waves in tokamak plasmas. *Plasma Phys. Control. Fusion* **55**, 095004.

NEMES, G. 2021 On the Borel summability of WKB solutions of certain Schrödinger-type differential equations. *J. Approx. Theory* **265**, 105562.

NEMES, G. 2025 On the Borel summability of formal solutions of certain higher-order linear ordinary differential equations. *J. Differ. Equ.* **415**, 645–700.

PICARD, G. & JOHNSTON, T.W. 1983 Absolute parametric instabilities in inhomogeneous plasmas. *Phys. Rev. Lett.* **51**, 574.

PORKOLAB, M. 1970 Nonlinear decay and instability of a nonuniform finite-amplitude plasma wave. *Phys. Fluids* **13**, 2054.

PORKOLÁB, M. 1972 Parametric instabilities in a Magnetic Field and possible applications to heating of plasmas. *Nucl. Fusion* **12**, 329–340.

Downloaded from https://www.cambridge.org/core. UNIVERSIDAD AUTONOMA METROPOLITANA, on 19 Nov 2026 at 15:26:59, subject to the Cambridge Core terms of use, available at https://www.cambridge.org/core/terms. https://doi.org/10.1017/S002237782610213X

QIU, Z., CHEN, L. & ZONCA, F. 2014 Excitation of kinetic geodesic acoustic modes by drift waves in nonuniform plasmas. *Phys. Plasmas* **21**, 022304.

QIU, Z. *et al.* 2025 Alpha particle confinement in CFEDR H-mode scenario. *Plasma Sci. Technol.* **27**, 104005.

REIMAN, A. 1979 Space-time evolution of nonlinear three-wave interactions. II. Interaction in an inhomogeneous medium. *Rev. Mod. Phys.* **51**, 311–330.

ROSENBERG, M.J. *et al.* 2018 Origins and scaling of hot-electron preheat in ignition-scale direct-drive inertial confinement fusion experiments. *Phys. Rev. Lett.* **120**, 055001.

ROSENBLUTH, M.N. 1972 Parametric instabilities in inhomogeneous media. *Phys. Rev. Lett.* **29**, 565–567.

SUEISHI, N., KAMATA, S., MISUMI, T. & ÜNSAL, M. 2020 On exact-WKB analysis, resurgent structure, and quantization conditions. *J. High Energy Phys.* **2020**, 114.

SUEISHI, N., KAMATA, S., MISUMI, T. & ÜNSAL, M. 2021 Exact-WKB, complete resurgent structure, and mixed anomaly in quantum mechanics on S1. *J. High Energy Phys.* **2021**, 96.

SUZUKI, T., TANIGUCHI, E. & IWAMURA, K. 2024 Exact WKB analysis for adiabatic discrete-level Hamiltonians. *Phys. Rev. A* **109**, 022225.

TAKEI, Y. 2017 WKB analysis and stokes geometry of differential equations. In *Analytic, Algebraic and Geometric Aspects of Differential Equations* (ed. G. Filipuk, Y. Haraoka & S. Michalik), pp. 263–304. Springer International Publishing.

TAYA, H., FUJIMORI, T., MISUMI, T., NITTA, M. & SAKAI, N. 2021 Exact WKB analysis of the vacuum pair production by time-dependent electric fields. *J. High Energy Phys.* **2021**, 82.

VOROS, A. 1983 The return of the quartic oscillator. The complex WKB method. *Ann. I'I.H.P., Phys. Théor.* **39**, 211–338.

WHITE, R., KAW, P., PESME, D., ROSENBLUTH, M.N., LAVAL, G., HUFF, R. & VARMA, R. 1974 Absolute parametric instabilities in inhomogeneous plasmas. *Nucl. Fusion* **14**, 45.

XIANG, N. & CARY, J.R. 2008 Second-harmonic generation of electron-bernstein waves in an inhomogeneous plasma. *Phys. Rev. Lett.* **100**, 085002.

YAN, F. 2022 Exact WKB and the quantum Seiberg-Witten curve for 4d $N = 2$ pure SU(3) Yang-Mills. Abelianization. *J. High Energy Phys.* **2022**, 164.

YAN, G.H. *et al.* 2024 Experimental investigation of PDI bifurcation of lower hybrid waves during electron density ramp-up in EAST. *Nucl. Fusion* **64**, 086018.

YANG, X. & GAO, Z. 2025 Analysis of parametric decay instabilities during helicon wave injection into tokamak plasma. *Phys. Plasmas* **32**, 122503.

ZHAO, A. & GAO, Z. 2013 Parameter study of parametric instabilities during lower hybrid wave injection into tokamaks. *Nucl. Fusion* **53**, 083015.

ZHOU, T., XIANG, N., GAN, C., WANG, X., JIA, G., CHEN, J., ZHAI, X. & HUANG, Y. 2022 Particle-in-cell simulations on parametric instability of the lower hybrid wave. *Phys. Plasmas* **29**, 102302.

ZHOU, T., XIANG, N., GAN, C. & XIA, T. 2025 Theoretical study of three-wave parametric instabilities in inhomogeneous plasma: a decoupling approach. *Phys. Plasmas* **32**, 072114.

ZINN-JUSTIN, J. 1981 Multi-instanton contributions in quantum mechanics. *Nucl. Phys. B* **192**, 125–140.

Downloaded from https://www.cambridge.org/core. UNIVERSIDAD AUTONOMA METROPOLITANA, on 19 Nov 2026 at 15:26:59, subject to the Cambridge Core terms of use, available at https://www.cambridge.org/core/terms. https://doi.org/10.1017/S002237782610213X